

Theory of birefringence correction for polarization-controlled CARS

YOUNG JONG LEE* 

Biosystems and Biomaterials Division, National Institute of Standards and Technology, Gaithersburg, MD 20899, USA

*youngjong.lee@nist.gov

Abstract: Polarization-controlled coherent Raman spectroscopy is used as a high-throughput method to characterize the anisotropic nature of a molecular system, such as the molecular orientation distribution. However, optical birefringence originating from the molecular anisotropy can cause the observed Raman spectrum to be significantly distorted, making it extremely challenging to obtain quantitative information from polarization Raman measurements. Here, the birefringence effect on the signal intensity and the spectral shape of a polarization-controlled coherent anti-Stokes Raman scattering (CARS) is theoretically described using a uniaxially symmetrical model system. Due to the complexity, the effect of phase delay in the incident lights is not considered but only that of the generated CARS signal is considered. A new analytical method is presented to eliminate the birefringence contribution from polarization-controlled CARS data by analyzing polarization intensity profiles and retrieving the resonant Raman susceptibility spectra. This method is tested with two sets of polarization-controlled CARS data simulated with various combinations of symmetries of multiple underlying Raman modes. The analysis result clearly demonstrates that the effect of birefringence can be corrected for polarization-controlled CARS data and the symmetry tensor elements of all underlying Raman modes can be quantitatively characterized.

1. Introduction

Polarization-controlled Raman spectroscopy has been widely used to characterize various types of anisotropic materials as a quantitative measurement method of molecular orientation distributions [1,2]. However, the extra dimension of polarization angle in addition to the long acquisition time makes spontaneous Raman impractical for general use imaging. As opposed to spontaneous Raman, coherent Raman microscopy approaches take advantage of stronger signals and faster imaging speed. Coherent anti-Stokes Raman scattering (CARS) microscopy has been widely used to image molecular anisotropy of spatially heterogeneous materials [3], including polymers [4,5], lipid layers [6–10], liquid crystals [11–13], fibers [14], inorganic crystals [15,16], and biological tissues [17]. Based on polarization-controlled CARS, experiments and theories have been reported to quantitatively determine parameters representing molecular orientation distribution functions, including not only the projected orientation but also the order parameters [8,18,19] and the out-of-plane orientation angle [11,20].

Polarization-controlled characterization of an anisotropic medium is often confounded by birefringence, which is the difference in a refractive index depending on the light polarization direction. Birefringence of a material is determined by various anisotropic properties of the material in a smaller length scale than the wavelength: for example, molecular orientation and crystallinity. As a result of birefringence, phase delay occurs between the two different polarization components of transmitted light. For example, common anisotropic organic materials (deformed polymers and aligned collagen fibrils) show birefringence in the range of 0.001 to 0.05 [21,22], which corresponds to a phase delay between $\frac{1}{10}\pi$ and 4π radian for 800 nm light passing through a 50 μm thick organic film. Phase delay between the two different polarization components results in a modified polarization state (e.g., polarization direction or ellipticity) of transmitted light. In nonlinear optical spectroscopy, a phase delay can result in more complex

spectral distortions, such as intensity drop, uneven baseline drift, and peak shift, due to coherent interactions between multiple photons of different colors [15]. For a quantitative discussion of polarization-controlled nonlinear spectroscopic results, the birefringence effect needs to be considered based on mathematical expressions of generation and propagation of a nonlinear signal in the presence of phase delay. Previously, the birefringence effect on second harmonic generation [23] and four-wave mixing microscopy [24] was described quantitatively using the symmetry angle and the phase delay measured *in situ*. However, the birefringence effect has not been fully exploited to explain the spectral distortion of polarization-controlled CARS.

This study presents a full description of the birefringence effect on CARS signals propagating through an anisotropic medium. A straightforward method is introduced to eliminate the birefringence effect from the polarization-controlled CARS spectra and to retrieve the resonant susceptibility spectra, which corresponds to the spontaneous Raman spectra. This method can determine the phase delay *in situ* from the observed nonresonant CARS data without requiring a separate polarimetric measurement. This new analysis method is tested with two different sets of simulation data of polarization-scanning broadband CARS spectral data, successfully reproducing the birefringence-free polarization Raman data. The results are discussed with two types of newly defined depolarization ratios of the resonant susceptibility for underlying Raman peaks, which can be useful for determining the group symmetry of the Raman modes as well as the molecular orientation distribution.

2. Theory of birefringence effect on polarization CARS

2.1. CARS signal propagation in a birefringent medium

A CARS signal is generated as a result of a coherent interaction of three electric fields: E_{pu} , E_{S} , and E_{pr} correspond to pump, Stokes, and probe transitions. More specifically, CARS nonlinear polarization, P_{CARS} , induced by the incident electric fields, generates a CARS signal, which travels toward a detector. The CARS nonlinear polarization is proportional to the incident electric fields, and the coefficient is called the CARS nonlinear susceptibility tensor, χ

$$P_{\text{CARS}} = \chi E_{\text{pu}} E_{\text{S}}^* E_{\text{pr}} \quad (1)$$

When a CARS signal is generated inside a birefringent medium, both the incident beams and the generated CARS signal experience the birefringence. Unlike a linear phenomenon, a description of the birefringence effect on this multicolor nonlinear phenomenon is very lengthy and complex because of many possible combinations of the three incident beams and their associated nonlinear susceptibility tensor elements. The full description becomes more complicated by not only wavelength-dependent phase delays of the multicolor incident beams but also the negative phase delay by the conjugate electric field for the Stokes transition. In this paper, therefore, the birefringence effect on a generated CARS signal propagating through a birefringent medium will be focused. The birefringence effect of the incident beams will be discussed in a future publication. Besides, it needs to be mentioned that the analysis is intended for polarization-controlled CARS imaging with moderate focusing. Then, the CARS signal is generated within a sufficiently thin slab, a spatial walk off that would go into treatment of a bulk CARS signal can be ignored. Also, polarization mixing due to tight focusing is not considered in this paper.

For the investigation of the polarization angle dependence, a CARS susceptibility tensor is expressed as $\chi = \chi(\omega)\alpha$, where $\chi(\omega)$ is the polarization-independent Raman line shape; and α is a normalized, fourth-rank tensor, which represents the orientation of the Raman mode. Similarly, the incident electric fields are also expressed as the product of the amplitude, $E(\omega)$, and the directional unit vector, \hat{e}_{E} . In this paper, only parallel, linear polarization is considered for all electric fields. As shown in the optical scheme of the polarization-controlled CARS system (Fig. 1), the input polarization is rotated by an achromatic half-wave plate, and the resulting

electric field directional unit vector can be expressed as $\hat{e}_E(\eta)$ a function of the polarization angle, η . The CARS polarization vector in Eq. (1) can be rewritten as a product of a frequency-dependent scalar and a polarization-angle dependent vector

$$\begin{aligned} \mathbf{P}_{\text{CARS}}(\omega, \eta) &= \left\{ \chi(\omega) E_{\text{pu}} E_{\text{S}}^* E_{\text{pr}} \right\} \left\{ \alpha \hat{e}_E^{\text{pu}}(\eta) \hat{e}_E^{\text{S}}(\eta) \hat{e}_E^{\text{pr}}(\eta) \right\} \\ &= \left\{ \chi(\omega) E_{\text{pu}} E_{\text{S}}^* E_{\text{pr}} \right\} \mathcal{A}(\eta) \end{aligned} \quad (2)$$

The i -th element of $\mathcal{A}(\eta)$ is expressed as $\mathcal{A}_i = \sum_{j,k,l} \alpha_{ijk} e_j^{\text{pu}} e_k^{\text{S}} e_l^{\text{pr}}$, where $i, j, k,$ and l are either 1 or 2, which are two in-plane components because the out-of-plane component of the electric fields is not considered in this paper.

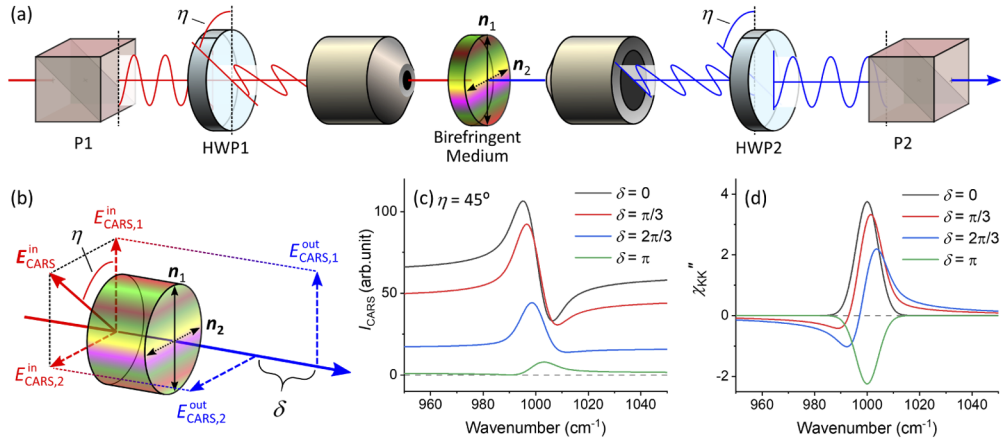


Fig. 1. (a) An optical scheme of a polarization-controlled CARS system. All incident beams are parallel polarized by the input polarizer (P1). The input achromatic half-wave plate (HWP1) rotates the input polarization at the sample by η . A CARS signal is generated at the entrance of the sample and then propagates through the birefringent medium. The fast axis (\hat{n}_1) of the birefringent medium is aligned parallel to the polarization direction of P1. The CARS output passes through the output waveplate (HWP2), which is synchronously rotated with HWP1, and through the output polarizer (P2), which is aligned parallel to P1. (b) An illustration of phase delay, δ , occurring to the CARS output electric field after it passes through the birefringent medium, which is assumed to be uniaxial in this paper. (c) CARS spectra simulated for various δ when $\eta = 45^\circ$. (d) Raman susceptibility spectra retrieved from (c) by the Kramers–Kronig (KK) method without birefringence correction.

The medium is considered to be uniaxial birefringent, which is the simplest and the most common type of birefringence. It is assumed that the χ is also uniaxial and parallel to the birefringence axis. Then, the fully linear polarization configuration of this study can be described with physical quantities projected onto two orthogonal axes: the fast axis, \hat{n}_1 , and the slow axis, \hat{n}_2 , as displayed in Fig. 1. When a CARS electric field, $E_{\text{CARS}}^{\text{in}}$, which is induced by \mathbf{P}_{CARS} , passes through the birefringent medium, phase delay (δ) occurs between the two projected electric fields, $E_{\text{CARS},1}^{\text{out}}$ and $E_{\text{CARS},2}^{\text{out}}$. The output electric field is expressed as

$$\mathbf{E}_{\text{CARS}}^{\text{out}} = (\mathbf{E}_{\text{CARS}}^{\text{in}} \cdot \hat{n}_1) \hat{n}_1 + e^{i\delta} (\mathbf{E}_{\text{CARS}}^{\text{in}} \cdot \hat{n}_2) \hat{n}_2 \quad (3)$$

The output electric field passes through analyzing polarization optics, which consist of an analyzing half-wave plate rotated parallel to the incident half-wave plate and a polarizer aligned

parallel to the incident polarizer. Then, the detected CARS signal intensity is expressed as

$$I_{\text{CARS}} \propto |\mathbf{E}_{\text{CARS}}^{\text{out}} \cdot \hat{\mathbf{e}}_E(\eta)|^2 \propto |(\mathbf{P}_{\text{CARS}} \cdot \hat{\mathbf{n}}_1)(\hat{\mathbf{n}}_1 \cdot \hat{\mathbf{e}}_E) + e^{i\delta}(\mathbf{P}_{\text{CARS}} \cdot \hat{\mathbf{n}}_2)(\hat{\mathbf{n}}_2 \cdot \hat{\mathbf{e}}_E)|^2 \quad (4)$$

The CARS intensity can also be expressed in a generalized form as

$$I_{\text{CARS}}(\omega, \eta, \delta) = K(\omega) |\mathcal{X}(\omega, \eta, \delta)|^2 \quad (5)$$

$K(\omega) \equiv C|E_{\text{pu}}E_{\text{s}}^*E_{\text{pr}}|^2$ is a coherent stimulation profile, where $|E_{\text{pu}}E_{\text{s}}^*E_{\text{pr}}|^2$ represents the product of the spectral convolution of the three electric fields, and C is the detector response function. $\mathcal{X}(\omega, \eta)$, an effective CARS susceptibility, can be expressed as a product of a frequency-dependent term and a polarization angle-dependent term as

$$\mathcal{X}(\omega, \eta, \delta) \equiv \chi(\omega) \{(\mathcal{A} \cdot \hat{\mathbf{n}}_1)(\hat{\mathbf{n}}_1 \cdot \hat{\mathbf{e}}_E) + e^{i\delta}(\mathcal{A} \cdot \hat{\mathbf{n}}_2)(\hat{\mathbf{n}}_2 \cdot \hat{\mathbf{e}}_E)\} \quad (6)$$

The nonlinear CARS susceptibility can be considered as a sum of a vibrationally resonant susceptibility and a nonresonant background susceptibility. A resonant susceptibility, $\mathcal{X}^r(\omega, \eta, \delta)$, is expressed as a complex number whose imaginary part is equivalent to the corresponding spontaneous Raman peak. A nonresonant susceptibility, $\mathcal{X}^{\text{nr}}(\eta, \delta)$, is represented with a frequency-independent real number.

$$I_{\text{CARS}}(\omega, \eta, \delta) = K(\omega) |\mathcal{X}^r(\omega, \eta, \delta) + \mathcal{X}^{\text{nr}}(\eta, \delta)|^2 \quad (7)$$

where

$$\mathcal{X}^r(\omega, \eta, \delta) = \sum_k \left\{ \chi_k'(\omega) + i\chi_k''(\omega) \right\} \left\{ (\mathcal{A}^k \cdot \hat{\mathbf{n}}_1)(\hat{\mathbf{n}}_1 \cdot \hat{\mathbf{e}}_E) + e^{i\delta}(\mathcal{A}^k \cdot \hat{\mathbf{n}}_2)(\hat{\mathbf{n}}_2 \cdot \hat{\mathbf{e}}_E) \right\} \quad (8)$$

$$\mathcal{X}^{\text{nr}}(\eta, \delta) = \chi^{\text{nr}} \left\{ (\mathcal{A}^{\text{nr}} \cdot \hat{\mathbf{n}}_1)(\hat{\mathbf{n}}_1 \cdot \hat{\mathbf{e}}_E) + e^{i\delta}(\mathcal{A}^{\text{nr}} \cdot \hat{\mathbf{n}}_2)(\hat{\mathbf{n}}_2 \cdot \hat{\mathbf{e}}_E) \right\} \quad (9)$$

where \mathcal{X}^r is expressed as a sum of resonant susceptibilities; χ_k' and χ_k'' are, respectively, the real and imaginary amplitudes of the resonant susceptibility of the k -th Raman mode; and χ^{nr} is the nonresonant susceptibility amplitude. Note that the superscript "r" is removed in describing the resonant susceptibility for simplicity while "nr" remains in superscripts for the nonresonant susceptibility. The nonresonant background susceptibility is generated by anisotropic electronic response of the medium, and its contribution often dominates over the coexisting resonant susceptibility. Due to difference in symmetry origin, polarization angle dependence is different between the nonresonant and resonant susceptibilities [25].

The coherent stimulation profile, $K(\omega)$, in Eq. (5) can be removed by a separate measurement of a CARS spectrum from reference material, e.g., glass and water, chosen to have a negligible resonant susceptibility compared to its nonresonant susceptibility. When a sample CARS spectrum is divided by the reference CARS spectrum, $I_{\text{ref}}(\omega) = K(\omega) |\chi_{\text{ref}}|^2$, where χ_{ref} is a real number,

$$\frac{I_{\text{CARS}}(\omega, \eta, \delta)}{I_{\text{ref}}(\omega)} = \left| \frac{\mathcal{X}^r(\omega, \eta, \delta)}{\chi_{\text{ref}}} + \frac{\mathcal{X}^{\text{nr}}(\eta, \delta)}{\chi_{\text{ref}}} \right|^2 \quad (10)$$

It is noted that the resonant and the nonresonant susceptibilities of a sample can be expressed as relative values to the nonresonant susceptibility of the reference material. Similar usage of the reference spectrum will be discussed later with the Kramers–Kronig (KK) phase retrieval method.

In the absence of birefringence, the imaginary component in $\left\{ \mathcal{X}^r(\omega, \eta) + \mathcal{X}^{\text{nr}}(\eta) \right\}$ is solely contributed by $\chi''(\omega)$ while the nonresonant susceptibility is a real, frequency-independent

number. This allows for the KK phase retrieval method to produce the $\chi''(\omega)$ spectrum, which corresponds to the spontaneous Raman spectrum [26], at each polarization angle. Then, a polarization angle profile of a specific Raman peak can be easily obtained and used for further analysis. However, in the presence of birefringence, phase delay in $e^{i\delta}$ mixes the real and imaginary susceptibilities and results in destructive interference of the CARS electric fields between the fast and slow axes. Therefore, the resulting KK-retrieved spectra significantly deviate from their corresponding birefringence-free KK-retrieved spectra.

Figures 1(c) and 1(d) show simulated CARS spectra and their direct KK-retrieved outputs, respectively, for various phase delays. The overall CARS intensity at the diagonal polarization angle ($\eta = 45^\circ$) is significantly reduced as the phase delay increases from 0 to π . The height and the shape of Raman peaks in the KK-retrieved spectra also change significantly with the phase delay, depending on both the input polarization angle and the group symmetry of each Raman mode. The interference can cause retrieved peaks to become negative, which is not physical, as shown in Fig. 1(d). This complex interference in polarization-controlled CARS signals from a birefringent medium makes it challenging for quantitative analyses. That is why only CARS spectra measured at two polarization angles (parallel to \hat{n}_1 and \hat{n}_2) can be used for spectral characterization without being affected by birefringence.

2.2. Nonresonant susceptibility and phase delay

In this section, it will be explained how to determine $\chi^{\text{nr}}(\eta, \delta)$ from the nonresonant CARS intensity. In the following section, such determined $\chi^{\text{nr}}(\eta, \delta)$ will be used to calculate $\chi^{\text{r}}(\eta, \delta)$. Also, a method to determine the phase delay *in situ* by analyzing the nonresonant CARS intensity will be introduced. As described for Eq. (2), the nonresonant polarization angle dependence vector, \mathcal{A}^{nr} , can be expressed with the corresponding nonresonant angular unit tensor, α^{nr} . Because only parallel polarization of the incident beams and the detected signal is considered, the two major elements of \mathcal{A}^{nr} along the fast and slow axes can be expressed as

$$\begin{aligned}\mathcal{A}_1^{\text{nr}}(\eta) &= \alpha_{1111}^{\text{nr}} \cos^3 \eta + (\alpha_{1122}^{\text{nr}} + \alpha_{1221}^{\text{nr}} + \alpha_{1212}^{\text{nr}}) \cos \eta \sin^2 \eta \\ \mathcal{A}_2^{\text{nr}}(\eta) &= (\alpha_{2211}^{\text{nr}} + \alpha_{2112}^{\text{nr}} + \alpha_{2121}^{\text{nr}}) \cos^2 \eta \sin \eta + \alpha_{2222}^{\text{nr}} \sin^3 \eta\end{aligned}\quad (11)$$

It should be noted that the eight nonzero elements of $\alpha_{ijkl}^{\text{nr}}$ are used because χ is assumed to be uniaxial. Then, $\alpha_{ijkl}^{\text{nr}}$ can be simplified into the four following susceptibility elements

$$\begin{aligned}\chi_{11}^{\text{nr}} &= \chi^{\text{nr}} \alpha_{1111}^{\text{nr}} \\ \chi_{12}^{\text{nr}} &= \chi^{\text{nr}} (\alpha_{1122}^{\text{nr}} + \alpha_{1221}^{\text{nr}} + \alpha_{1212}^{\text{nr}}) \\ \chi_{21}^{\text{nr}} &= \chi^{\text{nr}} (\alpha_{2211}^{\text{nr}} + \alpha_{2112}^{\text{nr}} + \alpha_{2121}^{\text{nr}}) \\ \chi_{22}^{\text{nr}} &= \chi^{\text{nr}} \alpha_{2222}^{\text{nr}}\end{aligned}\quad (12)$$

where χ_{12}^{nr} can be considered as equal to χ_{21}^{nr} because of the equivalency of the sub-components $\alpha_{ijkl}^{\text{nr}} = \alpha_{lkji}^{\text{nr}} = \alpha_{ikjl}^{\text{nr}} = \alpha_{lkji}^{\text{nr}}$. Then, $\chi^{\text{nr}}(\eta, \delta)$ can be simplified as

$$\begin{aligned}\chi^{\text{nr}}(\eta, \delta) &= \left[(\chi_{11}^{\text{nr}} - 2\chi_{12}^{\text{nr}} + \chi_{22}^{\text{nr}}) \cos^4 \eta + (2\chi_{12}^{\text{nr}} - 2\chi_{22}^{\text{nr}}) \cos^2 \eta + \chi_{22}^{\text{nr}} \right] \\ &+ (e^{i\delta} - 1) \left[(\chi_{22}^{\text{nr}} - \chi_{12}^{\text{nr}}) \cos^4 \eta + (\chi_{12}^{\text{nr}} - 2\chi_{22}^{\text{nr}}) \cos^2 \eta + \chi_{22}^{\text{nr}} \right]\end{aligned}\quad (13)$$

Then, the nonresonant background (NRB) CARS intensity, I_{NRB} , divided by the reference CARS intensity, I_{ref} , can be expressed as a sum of cosine functions as

$$\begin{aligned}\frac{I_{\text{NRB}}(\omega, \eta, \delta)}{I_{\text{ref}}(\omega)} &= \frac{|\chi^{\text{nr}}(\eta, \delta)|^2}{|\chi_{\text{ref}}|^2} \\ &= N_8 \cos^8 \eta + N_6 \cos^6 \eta + N_4 \cos^4 \eta + N_2 \cos^2 \eta + N_0\end{aligned}\quad (14)$$

where the polynomial coefficients N_{2n} can be expressed as combinations of χ_{ij}^{nr} and $\cos \delta$. It should be noted that χ_{ij}^{nr} is a relative value to χ_{ref} , hereafter.

When an observed polarization profile of I_{NRB}/I_{ref} is fitted with Eq. (14), the obtained coefficients N_{2n} can be used to determine the three unknown susceptibility elements (χ_{11}^{nr} , χ_{12}^{nr} , and χ_{22}^{nr}) and the phase delay, δ , based on the following relations

$$N_8 = (\chi_{11}^{nr})^2 + (\chi_{22}^{nr})^2 + 2(1 + \cos \delta) \left\{ (\chi_{12}^{nr})^2 - \chi_{11}^{nr} \chi_{12}^{nr} + \chi_{11}^{nr} \chi_{22}^{nr} - \chi_{12}^{nr} \chi_{22}^{nr} \right\} - 2\chi_{11}^{nr} \chi_{22}^{nr} \quad (15)$$

$$N_6 = -4(\chi_{22}^{nr})^2 + 2(1 + \cos \delta) \left\{ -2(\chi_{12}^{nr})^2 + \chi_{11}^{nr} \chi_{12}^{nr} - 2\chi_{11}^{nr} \chi_{22}^{nr} + 3\chi_{12}^{nr} \chi_{22}^{nr} \right\} + 4\chi_{11}^{nr} \chi_{22}^{nr} \quad (16)$$

$$N_4 = 6(\chi_{22}^{nr})^2 + 2(1 + \cos \delta) \left\{ (\chi_{12}^{nr})^2 + \chi_{11}^{nr} \chi_{22}^{nr} - 3\chi_{12}^{nr} \chi_{22}^{nr} \right\} - 2\chi_{11}^{nr} \chi_{22}^{nr} \quad (17)$$

$$N_2 = -4(\chi_{22}^{nr})^2 + 2(1 + \cos \delta) \left\{ \chi_{12}^{nr} \chi_{22}^{nr} \right\} \quad (18)$$

$$N_0 = (\chi_{22}^{nr})^2 \quad (19)$$

First, it is straightforward to find χ_{11}^{nr} and χ_{22}^{nr} from $I_{NRB}(0)$ and $I_{NRB}(\frac{\pi}{2})$, respectively

$$(\chi_{22}^{nr})^2 = N_0 \quad (20)$$

$$(\chi_{11}^{nr})^2 = N_T = N_8 + N_6 + N_4 + N_2 + N_0 \quad (21)$$

These two coefficients will be needed for birefringence correction of the resonant susceptibility in the next section.

From Eqs. (18) and (19), $\cos \delta$ can be expressed with χ_{12}^{nr} ,

$$\chi_{12}^{nr} = \frac{N_2 + 4(\chi_{22}^{nr})^2}{2(1 + \cos \delta)\chi_{22}^{nr}} = \frac{N_2 + 4N_0}{2(1 + \cos \delta)\sqrt{N_0}} \quad (22)$$

Inserting this into Eq. (17) yields a quadratic equation with respect to $\cos \delta$ as

$$\cos \delta = \left(\frac{N_4 + 3N_2 + 6N_0}{4\sqrt{N_T N_0}} - \frac{1}{2} \right) \pm \sqrt{\left(\frac{N_4 + 3N_2 + 6N_0}{4\sqrt{N_T N_0}} + \frac{1}{2} \right)^2 - \frac{(N_2 + 4N_0)^2}{4N_0\sqrt{N_T N_0}}} \quad (23)$$

Equation (23) generates two solutions for $\cos \delta$, and each $\cos \delta$ has two solutions for δ . Unfortunately, it is not possible to determine which δ value out of four solutions is the correct one only by this NRB intensity analysis. Additional measurements are needed to narrow down the choice of δ , such as a conventional polarimetric measurement [23,24]. In fact, phase delay can be measured by simultaneously measuring one of the incident beams while polarization-controlled CARS spectra are acquired. Once $\cos \delta$ is determined, χ_{12}^{nr} can also be determined from Eq. (17) although it is not used for birefringence correction in the following sections. It must be noted that, despite the degeneracy of δ , this method of Eq. (23) can measure the phase delay at the identical sample location for the same CARS generation configuration.

3. Birefringence correction

3.1. Resonant susceptibility

The resonant susceptibility can be discussed in a similar way to the nonresonant effective susceptibility except that the resonant susceptibility amplitude is a complex number. From Eq. (8),

$$\begin{aligned} \mathcal{X}^r(\omega, \eta, \delta) = \sum_k \left[\left\{ \chi'_k + i\chi''_k \right\} \left\{ (\alpha_{11}^k - 2\alpha_{12}^k + \alpha_{22}^k) \cos^4 \eta + (2\alpha_{12}^k - 2\alpha_{22}^k) \cos^2 \eta + \alpha_{22}^k \right\} \right. \\ \left. + (e^{i\delta} - 1) \left\{ \chi'_k + i\chi''_k \right\} \left\{ (\alpha_{22}^k - \alpha_{12}^k) \cos^4 \eta + (\alpha_{12}^k - 2\alpha_{22}^k) \cos^2 \eta + \alpha_{22}^k \right\} \right] \end{aligned} \quad (24)$$

where $\alpha_{11}^k = \alpha_{1111}^k$; $\alpha_{12}^k = (\alpha_{1122}^k + \alpha_{1221}^k + \alpha_{1212}^k)$; $\alpha_{21}^k = (\alpha_{2211}^k + \alpha_{2112}^k + \alpha_{2121}^k)$; and $\alpha_{22}^k = \alpha_{2222}^k$. Also, α_{12}^k is considered to be equal to α_{21}^k based on the equivalency of the permuted sub-component, similar to the relation for nonresonant tensor elements of $\alpha_{12}^{nr} = \alpha_{21}^{nr}$. Then, for simplicity, the real and the imaginary susceptibility amplitudes are combined with the polarization-dependent tensor elements as

$$\begin{aligned} \chi'_{ij} &= \sum_k \chi'_k \alpha_{ij}^k \\ \chi''_{ij} &= \sum_k \chi''_k \alpha_{ij}^k \end{aligned} \quad (25)$$

Back to the CARS intensity of Eq. (10), the total CARS intensity divided by the reference CARS intensity can be expressed as a sum of cosine polynomials.

$$\frac{I_{\text{CARS}}(\omega, \eta, \delta)}{I_{\text{ref}}(\omega)} = M_8 \cos^8 \eta + M_6 \cos^6 \eta + M_4 \cos^4 \eta + M_2 \cos^2 \eta + M_0 \quad (26)$$

Then, CARS spectra corresponding to the fast axis ($\eta = 0$) and the slow axis ($\eta = \frac{\pi}{2}$) can be expressed straightforwardly as

$$\frac{I_{\text{CARS}}(\omega, 0, \delta)}{I_{\text{ref}}(\omega)} = M_T = M_8 + M_6 + M_4 + M_2 + M_0 = \left(\chi'_{11} + \chi_{11}^{nr} \right)^2 + \left(\chi''_{11} \right)^2 \quad (27)$$

$$\frac{I_{\text{CARS}}(\omega, \frac{\pi}{2}, \delta)}{I_{\text{ref}}(\omega)} = M_0 = \left(\chi'_{22} + \chi_{22}^{nr} \right)^2 + \left(\chi''_{22} \right)^2 \quad (28)$$

It is noted that, at these two polarization angles, there is no birefringence-caused interference.

3.2. Kramers–Kronig (KK) retrieval

The KK phase retrieval method uses the phase relationship between the CARS signal and the NRB to extract the imaginary component of the total CARS susceptibility from the total CARS intensity spectrum [27,28]. In KK retrieval, the phase of the total CARS/ref susceptibility, $\phi_{\text{CARS/ref}}$, can be calculated by the Hilbert transform with $I_{\text{CARS}}(\omega, \eta, \delta)/I_{\text{ref}}(\omega, \delta)$ as

$$\begin{aligned} \phi_{\text{CARS/ref}}(\omega, \eta, \delta) &= \mathcal{H} \left\{ \frac{1}{2} \ln \frac{I_{\text{CARS}}(\omega, \eta, \delta)}{I_{\text{ref}}(\omega)} \right\} \\ &= \arg \{ \mathcal{X}(\omega, \eta, \delta) \} - \arg \{ \chi_{\text{ref}} \} \approx \arg \{ \mathcal{X}(\omega, \eta) \} \end{aligned} \quad (29)$$

where $\hat{\mathcal{H}}$ is the Hilbert transform, and $\arg\{ \}$ denotes the angle of the complex value. Then, the KK-retrieved spectrum, $\chi_{\text{KK}}(\omega, \eta, \delta)$, can be expressed as

$$\begin{aligned}\chi_{\text{KK}}(\omega, \eta) &= \hat{\mathcal{K}} \left\{ \frac{I_{\text{CARS}}(\omega, \eta, \delta)}{I_{\text{ref}}(\omega)} \right\} = \sqrt{\frac{I_{\text{CARS}}(\omega, \eta, \delta)}{I_{\text{ref}}(\omega)}} e^{i\phi_{\text{CARS/ref}}} \\ &= \frac{|\mathcal{X}(\omega, \eta, \delta)| e^{i \arg\{\mathcal{X}(\omega, \eta, \delta)\}}}{|\chi_{\text{ref}}|} = \frac{\mathcal{X}(\omega, \eta, \delta)}{|\chi_{\text{ref}}|}\end{aligned}\quad (30)$$

where χ_{KK} is a relative value of \mathcal{X} to χ^{ref} .

As briefly mentioned earlier, in the presence of phase delay, the imaginary component of the nonresonant susceptibility contribution becomes nonzero (See Eq. (13)), and the real and the imaginary component of the resonant susceptibility mix with each other. When birefringence mixes the real and imaginary components, it breaks causality in the time domain, which is the basic requirement of the KK phase retrieval. Therefore, in birefringent samples, only CARS spectra corresponding to $\eta = 0$ and $\eta = \frac{\pi}{2}$ can be processed with the KK phase retrieval because the spectra are not affected by birefringence-induced interference. Then, from Eqs. (27) and (28), the CARS spectra at $\eta = 0$ and $\eta = \frac{\pi}{2}$ can be constructed with the fitting coefficients of cosine polynomials introduced in Eq. (26). A direct KK operation, denoted as $\hat{\mathcal{K}}\{ \}$, on the two CARS spectra will generate the total CARS susceptibility as

$$\chi_{\text{KK}}(\omega, 0, \delta) = \hat{\mathcal{K}}\{M_{\text{T}}\} = \left\{ \chi'_{11} + \chi_{11}^{\text{nr}} \right\} + i \left\{ \chi''_{11} \right\} \quad (31)$$

$$\chi_{\text{KK}}(\omega, \frac{\pi}{2}, \delta) = \hat{\mathcal{K}}\{M_0\} = \left\{ \chi'_{22} + \chi_{22}^{\text{nr}} \right\} + i \left\{ \chi''_{22} \right\} \quad (32)$$

From the real and the imaginary components of the KK outputs,

$$\chi''_{11} = \text{Im} \left[\hat{\mathcal{K}}\{M_{\text{T}}\} \right] \quad (33)$$

$$\chi'_{11} = \text{Re} \left[\hat{\mathcal{K}}\{M_{\text{T}}\} \right] - \chi_{11}^{\text{nr}} \quad (34)$$

$$\chi''_{22} = \text{Im} \left[\hat{\mathcal{K}}\{M_0\} \right] \quad (35)$$

$$\chi'_{22} = \text{Re} \left[\hat{\mathcal{K}}\{M_0\} \right] - \chi_{22}^{\text{nr}} \quad (36)$$

where χ_{11}^{nr} and χ_{22}^{nr} are separately determined earlier by analyzing $I_{\text{NRB}}(\eta)$ in the previous section.

3.3. Depolarization ratios

In spontaneous Raman spectroscopy, depolarization ratio, defined as the ratio of parallel and perpendicular polarization Raman intensities, has been used to characterize the group symmetry of a Raman mode [29]. Similarly, in coherent Raman spectroscopy, the depolarization ratio is used to describe the symmetry of a nonlinear susceptibility isotropic media [24,30–32] as well as anisotropic media [5,15]. In this paper, two different depolarization ratios are defined as the ratios of nonlinear CARS susceptibility tensor elements and use them to characterize Raman modes. The depolarization ratios will also be used to eliminate the birefringence effect and to reconstruct a birefringence-corrected polarization Raman spectrum.

In this CARS system from a uniaxial birefringent material, the imaginary component of a resonant susceptibility tensor has three nonzero elements, χ''_{11} , χ''_{12} , and χ''_{22} , which are used definition of two different depolarization ratios as

$$\beta \equiv \chi''_{22} / \chi''_{11}, \quad \gamma \equiv \chi''_{12} / \chi''_{11} \quad (37)$$

where β is the *diagonal* depolarization ratio, and γ is the *off-diagonal* depolarization ratio. In theory, the identical ratios can be calculated with the real components, χ'_{11} , χ'_{12} , and χ'_{22} . However, in reality, the dispersive functional shape of a real component results in numerical singularity due to division-by-zero at the resonant frequency.

The values of β can be easily determined from the direct KK-retrieved spectra shown in from Eqs. (33) and (35) as

$$\beta(\omega) = \text{Im} \left[\hat{\mathcal{K}} \left\{ M_0 \right\} \right] / \text{Im} \left[\hat{\mathcal{K}} \left\{ M_T \right\} \right] \quad (38)$$

Unlike β , however, γ requires very long and complicated expressions of M_{2n} . To find a way to relate γ with M_{2n} , it is very useful to replace $(\chi'_{ij} + \chi_{ij}^{\text{nr}}) + i\chi''_{ij}$ with χ_{ij} and to treat it like a vector with the following definitions

$$|\chi_{ij}|^2 \equiv (\chi'_{ij} + \chi_{ij}^{\text{nr}})^2 + (\chi''_{ij})^2 \quad (39)$$

$$\langle \chi_{ij} \cdot \chi_{kl} \rangle \equiv (\chi'_{ij} + \chi_{ij}^{\text{nr}})(\chi'_{kl} + \chi_{kl}^{\text{nr}}) + \chi''_{ij}\chi''_{kl} \quad (40)$$

$$\langle \chi_{ij}^\dagger \cdot \chi_{kl} \rangle \equiv \chi''_{ij}(\chi'_{kl} + \chi_{kl}^{\text{nr}}) - (\chi'_{ij} + \chi_{ij}^{\text{nr}})\chi''_{kl} \quad (41)$$

Then, Eq. (24) can be simplified as

$$\begin{aligned} \mathcal{X} &= \mathcal{X}^r + \mathcal{X}^{\text{nr}} \\ &= \chi_{11} \cos^4 \eta + \chi_{12}(1 + e^{i\delta}) \cos^2 \eta \sin^2 \eta + \chi_{22} e^{i\delta} \sin^4 \eta \end{aligned} \quad (42)$$

From Eq. (26),

$$\frac{I_{\text{CARS}}}{I_{\text{ref}}} = \frac{1}{\chi_{\text{ref}}} |\chi_{11} \cos^4 \eta + \chi_{12}(1 + e^{i\delta}) \cos^2 \eta \sin^2 \eta + \chi_{22} e^{i\delta} \sin^4 \eta|^2 \quad (43)$$

Then, M_{2n} can be expressed as

$$\begin{aligned} M_8 &= |\chi_{11}|^2 + 2|\chi_{12}|^2 + |\chi_{22}|^2 - 2\langle \chi_{11} \cdot \chi_{12} \rangle - 2\langle \chi_{12} \cdot \chi_{22} \rangle \\ &\quad + 2 \cos \delta \left(|\chi_{12}|^2 - \langle \chi_{11} \cdot \chi_{12} \rangle + \langle \chi_{11} \cdot \chi_{22} \rangle - \langle \chi_{12} \cdot \chi_{22} \rangle \right) \\ &\quad + 2 \sin \delta \left(-\langle \chi_{11}^\dagger \cdot \chi_{12} \rangle + \langle \chi_{11}^\dagger \cdot \chi_{22} \rangle - \langle \chi_{12}^\dagger \cdot \chi_{22} \rangle \right) \end{aligned} \quad (44)$$

$$\begin{aligned} M_6 &= -4|\chi_{12}|^2 - 4|\chi_{22}|^2 + 2\langle \chi_{11} \cdot \chi_{12} \rangle + 6\langle \chi_{12} \cdot \chi_{22} \rangle \\ &\quad + 2 \cos \delta \left(-2|\chi_{12}|^2 + \langle \chi_{11} \cdot \chi_{12} \rangle - 2\langle \chi_{11} \cdot \chi_{22} \rangle + 3\langle \chi_{12} \cdot \chi_{22} \rangle \right) \\ &\quad + 2 \sin \delta \left(\langle \chi_{11}^\dagger \cdot \chi_{12} \rangle - 2\langle \chi_{11}^\dagger \cdot \chi_{22} \rangle + 3\langle \chi_{12}^\dagger \cdot \chi_{22} \rangle \right) \end{aligned} \quad (45)$$

$$\begin{aligned} M_4 &= 2|\chi_{12}|^2 + 6|\chi_{22}|^2 - 6\langle \chi_{12} \cdot \chi_{22} \rangle \\ &\quad + 2 \cos \delta \left(|\chi_{12}|^2 + \langle \chi_{11} \cdot \chi_{22} \rangle - 3\langle \chi_{12} \cdot \chi_{22} \rangle \right) \\ &\quad + 2 \sin \delta \left(\langle \chi_{11}^\dagger \cdot \chi_{22} \rangle - 3\langle \chi_{12}^\dagger \cdot \chi_{22} \rangle \right) \end{aligned} \quad (46)$$

$$M_2 = -4|\chi_{22}|^2 + 2\langle\chi_{12} \cdot \chi_{22}\rangle + 2 \cos \delta \langle\chi_{12} \cdot \chi_{22}\rangle + 2 \sin \delta \langle\chi_{12}^\dagger \cdot \chi_{22}\rangle \quad (47)$$

$$M_0 = |\chi_{22}|^2 \quad (48)$$

By rearranging the coefficients, the following simple expressions are obtained

$$M_a = \frac{1}{2}(M_6 + 2M_4 + 3M_2 + 4M_0) = (1 + \cos \delta)\langle\chi_{11} \cdot \chi_{12}\rangle + \sin \delta \langle\chi_{11}^\dagger \cdot \chi_{12}\rangle \quad (49)$$

$$M_b = \frac{1}{2}(M_2 + 4M_0) = (1 + \cos \delta)\langle\chi_{12} \cdot \chi_{22}\rangle + \sin \delta \langle\chi_{12}^\dagger \cdot \chi_{22}\rangle \quad (50)$$

In order to calculate χ_{12}'' , Eq. (49) is rearranged using the definitions of Eqs. (40) and (41)

$$M_a = \left\{ (1 + \cos \delta)(\chi'_{11} + \chi_{11}^{nr}) + \sin \delta \chi''_{11} \right\} (\chi'_{12} + \chi_{12}^{nr}) + \left\{ (1 + \cos \delta)\chi''_{11} - \sin \delta(\chi'_{11} + \chi_{11}^{nr}) \right\} \chi''_{12} \quad (51)$$

Similarly, Eq. (50) is rearranged

$$M_b = \left\{ (1 + \cos \delta)(\chi'_{22} + \chi_{22}^{nr}) - \sin \delta \chi''_{22} \right\} (\chi'_{12} + \chi_{12}^{nr}) + \left\{ (1 + \cos \delta)\chi''_{22} + \sin \delta(\chi'_{22} + \chi_{22}^{nr}) \right\} \chi''_{12} \quad (52)$$

After $(\chi'_{22} + \chi_{22}^{nr})$ is eliminated from Eqs. (51) and (52), χ''_{12} can be determined as

$$\chi''_{12} = \frac{PM_a - QM_b}{2(1 + \cos \delta) \left[\cos \delta \langle\chi_{11}^\dagger \cdot \chi_{22}\rangle - \sin \delta \langle\chi_{11} \cdot \chi_{22}\rangle \right]} \quad (53)$$

where

$$P = (1 + \cos \delta)(\chi'_{22} + \chi_{22}^{nr}) - \sin \delta \chi''_{22} \quad (54)$$

$$Q = (1 + \cos \delta)(\chi'_{11} + \chi_{11}^{nr}) + \sin \delta \chi''_{11} \quad (55)$$

Then, γ can be calculated as

$$\gamma = \frac{\chi''_{12}}{\chi''_{11}} = \frac{PM_a - QM_b}{2(1 + \cos \delta)\chi''_{11} \left[\cos \delta \langle\chi_{11}^\dagger \cdot \chi_{22}\rangle - \sin \delta \langle\chi_{11} \cdot \chi_{22}\rangle \right]} \quad (56)$$

It is noted that the birefringence-corrected polarization Raman spectrum of Eq. (57) is non-iteratively determined at each frequency independently without requiring any knowledge of the shape or bandwidth of underlying Raman peaks. At the same time, it also needs to be reiterated that the degeneracy in δ can result in multiple solutions of γ unless δ is independently confirmed by a separate polarimetric measurement, as mentioned in Section 2.2. The two depolarization ratios, β and γ , indicate the symmetrical nature of the interrogated Raman mode quantitatively. Finally, using β and γ determined from Eqs. (38) and (56), respectively, the birefringence-corrected polarization Raman spectrum, $\chi''_{BC}(\omega, \eta)$, can be reconstructed as

$$\chi''_{BC}(\omega, \eta) = \chi''_{11}(\omega) \left[\left\{ 1 - 2\gamma(\omega) + \beta(\omega) \right\} \cos^4 \eta + 2 \left\{ \gamma(\omega) - \beta(\omega) \right\} \cos^2 \eta + \beta(\omega) \right] \quad (57)$$

The coefficients of $\cos^{2n} \eta$ can be used to characterize the molecular orientation distribution function furthermore [20].

4. Application to polarization CARS simulation data

This newly developed analytical method of birefringence correction is tested with two simulation datasets of polarization-controlled CARS spectra. The first dataset is intended to show if the result matches the expected output parameters. The second dataset represents more realistic data, which contain noise and are acquired at discrete polarization angles.

4.1. Two overlapping peaks with different depolarization ratios

The first dataset is generated with two Raman peaks that are closely located to each other but with different depolarization ratios. One Raman peak has a greater CARS susceptibility along the fast axis while the other Raman peak, along the slow axis. The nonresonant susceptibility is assumed to be stronger along the slow axis. Figure 2(a) shows the total CARS spectra at four different polarization angles. Due to destructive interference, the CARS intensity at diagonal polarization angles ($\eta = 30^\circ$ and $\eta = 60^\circ$) are found lower than the parallel or perpendicular polarization angles ($\eta = 0^\circ$ and $\eta = 90^\circ$). The interference effect is more clearly shown in the polar plot of the total CARS intensity in Fig. 2(b). The interference still remains in the uncorrected susceptibility retrieved by the direct KK method, as shown as dips near $\eta = 45^\circ$ in the polar plots of the uncorrected susceptibility at the peak frequencies of Fig. 2(d). On the other hand, the birefringence-corrected susceptibility, calculated with Eq. (57), show no dips in the polar plots in Fig. 2(f). Also, the peaks in Fig. 2(e) can be deconvoluted into two original Gaussian peaks that have common center frequencies and the common FWHMs for different η , which is not the case in the uncorrected susceptibility plots in Fig. 2(c).

As mentioned before, during the calculation, two depolarization ratios, β and γ , are calculated and used for birefringence correction at each frequency. Figures 2(h) and 2(g) show the plots of β and γ , respectively. The plots show that both depolarization ratios stay constant where a single peak is dominant and show a smooth transition from one value to the other value where the two peaks are overlapping. Those flat values are very close to the original input values, indicated as the horizontal dashed lines. The birefringence correction results show that this analytical method can not only reproduce the birefringence-free polarization Raman spectra but also provide new metrics of the Raman mode symmetry even where multiple Raman modes overlap.

4.2. Noise-added CARS spectra at discrete polarization angles

The second dataset is designed to simulate more realistic polarization-controlled CARS data. Figure 3 shows six CARS spectra calculated for different polarization angles. Also, shot noise is added to a CARS signal. For emulation of anisotropic organic material, a set of input peak parameters are inferred from the polarization-controlled Raman spectra observed from a semi-crystalline polyethylene film [4]. The simulation dataset consists of eight Gaussian peaks with four different types of Raman symmetries, of which the depolarization ratios are arbitrarily set for the calculation purpose.

At each frequency, six CARS intensities are fitted with the cosine polynomials of Eq. (26). Figures 3(b)–3(e) show the CARS intensity data points and the cosine polynomial fitting curves at four representative frequencies. The shifted phase of η indicates that the optical axis of the sample is tilted by 20° . Nonresonant susceptibilities are determined by the cosine polynomial fitting of the average value of the CARS intensities at 700 cm^{-1} and 1850 cm^{-1} , which are assumed to have a negligible contribution from resonant susceptibility compared to nonresonant one. While the nonresonant susceptibilities are determined, the phase delay for this dataset is determined as 92.8° , which is close to the input value of 90° . Using the coefficients, $M^{(2n)}$, two CARS spectra corresponding to the fast axis and the slow axis are calculated from Eqs. (27) and (28). Their KK results are converted into the real and the imaginary components of resonant susceptibilities from Eqs. (33)–(36). These results and M_{2n} are used to calculate the

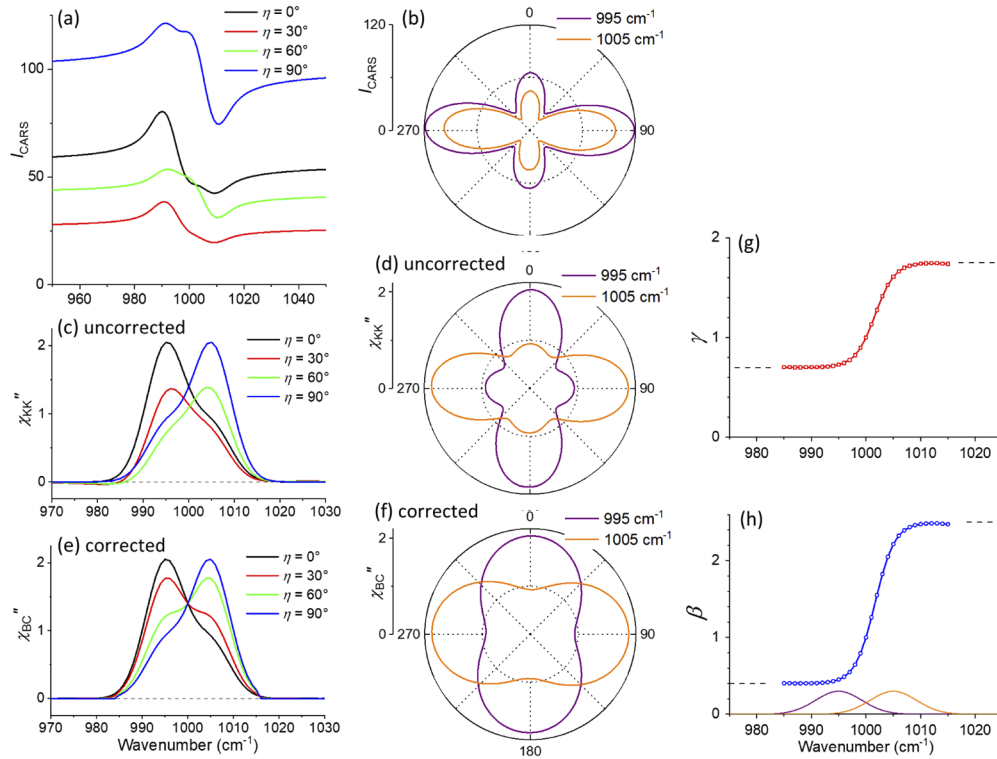


Fig. 2. (a) CARS spectra simulated at various polarization angles using two overlapping Raman peaks with different polarization tensors using the following input parameters: $\delta = \frac{2}{3}\pi$; for the NRB: $\chi_{11}^{\text{nr}} = 7.5$, $\chi_{12}^{\text{nr}} = 9$, and $\chi_{22}^{\text{nr}} = 10$. Gaussian functions are used for the imaginary component of the two peaks centered at 995 cm^{-1} and 1005 cm^{-1} with the full-width-half-maximum (FWHM) of 10 cm^{-1} . For the 995 cm^{-1} peak: $\chi_{11} = 2$, $\chi_{12} = 1.4$, and $\chi_{22} = 0.8$. For the 1005 cm^{-1} peak: $\chi_{11} = 0.8$, $\chi_{12} = 1.4$, and $\chi_{22} = 2$. (b) Polar plots of CARS intensity at the two center frequencies. The increment of (c) Uncorrected resonant susceptibility retrieved by the direct KK retrieval method of Eq. (30) without birefringence correction. (d) Polar plots of the uncorrected resonant susceptibilities at the two center frequencies. (e) Resonant susceptibility reconstructed after birefringence correction using Eq. (57), which used a phase delay ($\cos \delta = -0.50$) determined from the CARS data with Eq. (23). (f) Polar plots of the birefringence-corrected resonant susceptibility at the two center frequencies. (g) and (h) Spectra of depolarization ratios, γ and β . The values are calculated where χ_{11}'' is above a threshold of 0.02. The dashed horizontal lines next to the ordinates in (g) and (h) indicate the expected values based on input parameters.

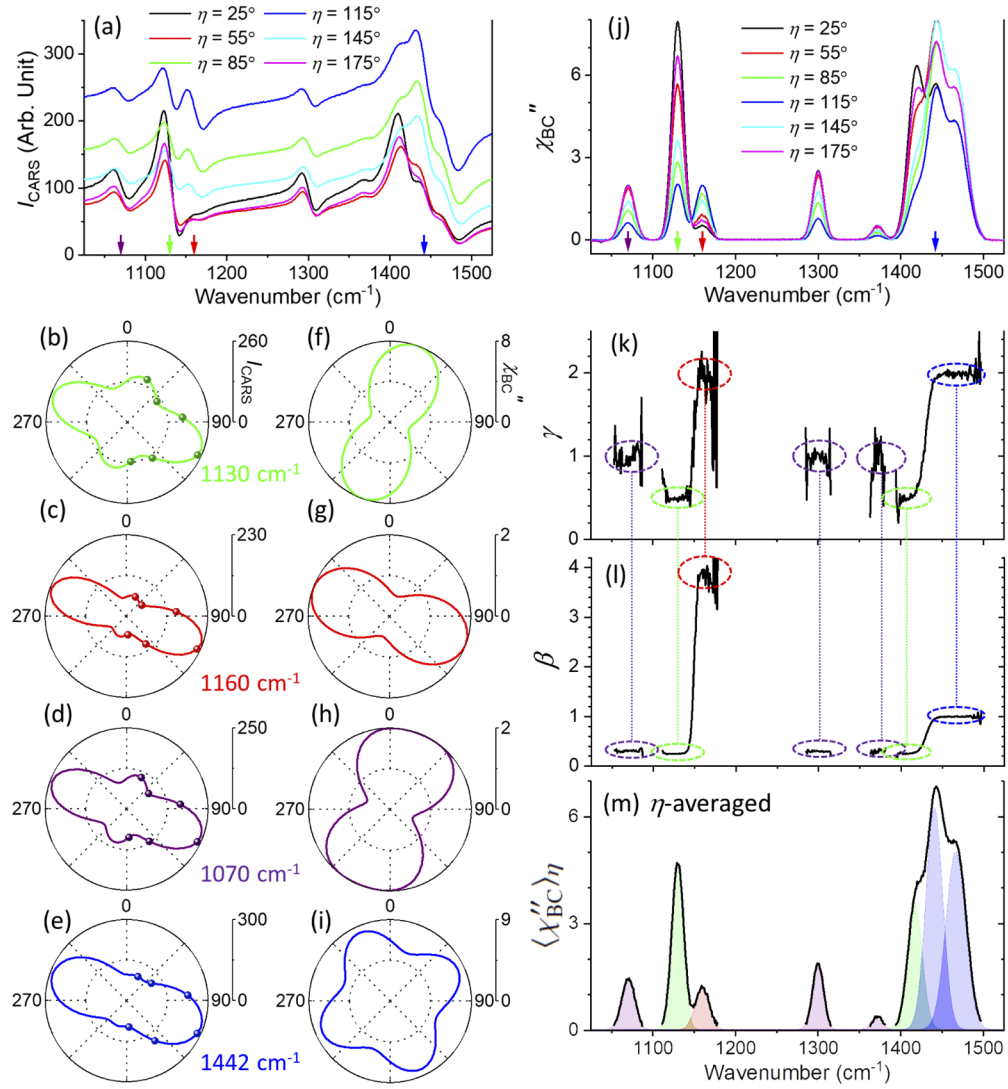


Fig. 3. (a) Six CARS spectra calculated with 30° increment of η . A random noise of 5% of $\sqrt{I_{\text{CARS}}}$ is added a CARS signal, mimicking a shot noise. The input phase delay used for simulation is $\delta = \pi/2$. (b)–(e) Six data points at the specified frequencies (the scatters) are fitted with Eq. (26) (the solid lines). (f)–(i) Birefringence-corrected resonant susceptibility at the corresponding frequencies. (j) Birefringence-corrected resonant susceptibility spectra at the six polarization angles. (k) and (l) Plots of the two depolarization ratios, β and γ , respectively, where spectral data are used only when χ''_{11} or χ''_{22} is above a threshold of 0.1. (m) The polarization angle-averaged susceptibility calculated with Eq. (57). The four different colors of polar plots correspond to the four different pairs of β and γ , which are also indicated as the arrows in (a) and (j).

depolarization ratios at each frequency, which are shown in Figs. 3(k) and 3(l), respectively. Then, finally, the birefringence-corrected polarization-dependent resonant susceptibility spectra can be calculated from Eq. (57). Figure 3(j) shows the birefringence-corrected resonant susceptibility spectra at different η , and Figs. 3(f)–3(i) show polar plots of birefringence-corrected resonant susceptibility at the frequencies corresponding to Figs. 3(b)–3(e).

From the spectra of depolarization ratios in Figs. 3(k) and 3(l), it is noted that noise propagation to γ appears to be greater than to β probably because of the more complex formulation of γ with the fitting parameters and the resonant and nonresonant susceptibilities. Regarding the implication of the symmetry of a Raman mode, the peak centered at 1130 cm^{-1} (green-colored) shows that $\beta = 0.25$ and $\gamma = 0.5$. This means that χ''_{11} is greater than χ''_{12} and χ''_{22} and that the Raman mode is aligned along \mathbf{n}_1 and the off-diagonal tensor element is relatively small. Similar values of β and γ are found for the 1418 cm^{-1} (green-colored), which makes the peak treated as the same type of Raman symmetry as the 1130 cm^{-1} peak. On the other hand, the weak 1160 cm^{-1} peak shows a quite different value in $\beta = 4$, indicating that the Raman mode is perpendicular to \mathbf{n}_1 . Although γ is larger than one, it is still smaller than β , which means that the off-diagonal tensor element, χ''_{12} , is smaller than the dominant diagonal element, χ''_{22} .

The Raman symmetry of the (purple-colored) peaks centered at 1070 cm^{-1} , 1300 cm^{-1} , and 1372 cm^{-1} are different from the 1130 cm^{-1} peak (green-colored). While both groups show χ''_{11} is the dominant diagonal elements, the off-diagonal element, χ''_{12} , is comparable to the dominant diagonal element, χ''_{11} . Therefore, the 1130 cm^{-1} mode and the 1070 cm^{-1} mode must be considered as different Raman symmetries. The peaks centered at 1442 cm^{-1} and 1468 cm^{-1} (blue-colored) exhibits a quite different behavior from the other peaks in that the off-diagonal element, χ''_{12} , is two times greater than the diagonal elements, χ''_{11} and χ''_{22} , which is shown as the maximum value at the diagonal polarization angle in the corresponding polar plot (See Fig. 3(i)). The birefringence correction results shown in Fig. 3 suggest that the analytical method works well only with six polarization-controlled CARS spectra in the presence of noise.

The output of this birefringence-correction method can also be used to generate a polarization-averaged Raman spectrum, which is considered as system-independent. By integrating Eq. (57) with respect to η , the polarization-averaged Raman spectrum is expressed as

$$\langle \chi''_{BC} \rangle_{\eta}(\omega) = \frac{1}{\pi} \int_0^{\pi} \chi''_{BC}(\omega, \eta) d\eta = \text{Im} \left[\hat{\mathcal{K}} \left\{ M_T \right\} \right] \left(\frac{3}{8} + \frac{1}{4}\gamma + \frac{3}{8}\beta \right) \quad (58)$$

This can be considered as the Raman spectrum expected from uniformly distributed molecules in the polarization plane when linearly polarized excitation and detection are used. However, it should be noted that a polarization-averaged Raman spectrum can change if the average out-of-plane angle is different. Therefore, a polarization-averaged Raman spectrum can be used to determine the average out-of-phase angle of a probed pixel in a polarization-controlled CARS image.

5. Conclusion

I have analytically described the birefringence effect on a polarization-controlled CARS output and have introduced a new method to eliminate the birefringence contribution from polarization-controlled CARS data by using cosine polynomial fittings and the KK phase retrieval method. Specifically, the birefringence effect on a CARS signal propagating through a uniaxially symmetrical medium has been considered. This new analytical method does not require any iterative optimization or *a priori* knowledge of the shapes, positions, or group symmetries of underlying Raman peaks. In addition to birefringence-corrected Raman spectra, two depolarization ratios are calculated at each frequency, and they can be used to characterize the molecular symmetry of the underlying Raman mode and the orientation distribution. This method is tested with two sets

of polarization-controlled CARS data simulated with various combinations of symmetries of the underlying Raman modes. The analysis results not only highlight birefringence correction in polarization-controlled CARS analysis but also unravel the symmetry parameters of individual Raman modes.

Acknowledgement

The author thanks Lee Richter for a critical review of the manuscript.

Disclosures

The author declares no conflicts of interest.

References

1. M. Tanaka and R. J. Young, "Polarised Raman spectroscopy for the study of molecular orientation distributions in polymers," *J. Mater. Sci.* **41**(3), 963–991 (2006).
2. M. Richard-lacroix and C. Pellerin, "Accurate New Method for Molecular Orientation Quantification Using Polarized Raman Spectroscopy," *Macromolecules* **46**(14), 5561–5569 (2013).
3. S. H. Parekh and K. F. Domke, "Watching orientational ordering at the nanoscale with coherent anti-Stokes Raman microscopy," *Chem. - Eur. J.* **19**(36), 11822–11830 (2013).
4. Y. J. Lee, C. R. Snyder, A. M. Forster, M. T. Cicerone, and W.-I. L. Wu, "Imaging the Molecular Structure of Polyethylene Blends with Broadband Coherent Raman Microscopy," *ACS Macro Lett.* **1**(11), 1347–1351 (2012).
5. C. Zhang, J. Wang, B. Ding, and J. Jasensky, "Quantitative spectral analysis of coherent anti-Stokes Raman scattering signals: C-H stretching modes of the methyl group," *J. Phys. Chem. B* **118**(27), 7647–7656 (2014).
6. A. P. Kennedy, J. Sutcliffe, and J.-X. Cheng, "Molecular Composition and Orientation in Myelin Figures Characterized by Coherent Anti-Stokes Raman Scattering Microscopy," *Langmuir* **21**(14), 6478–6486 (2005).
7. G. W. H. Wurpel, H. A. Rinia, and M. Müller, "Imaging orientational order and lipid density in multilamellar vesicles with multiplex CARS microscopy," *J. Microsc.* **218**(1), 37–45 (2005).
8. C. Zhang, J. Wang, J. Jasensky, and Z. Chen, "Molecular Orientation Analysis of Alkyl Methylene Groups from Quantitative Coherent Anti-Stokes Raman Scattering Spectroscopy," *J. Phys. Chem. Lett.* **6**(8), 1369–1374 (2015).
9. M. Hofer, N. K. Balla, and S. Brasselet, "High-speed polarization-resolved coherent Raman scattering imaging," *Optica* **4**(7), 795–801 (2017).
10. C. Cleff, A. Gasecka, P. Ferrand, H. Rigneault, S. Brasselet, and J. Duboisset, "Direct imaging of molecular symmetry by coherent anti-Stokes Raman scattering," *Nat. Commun.* **7**(1), 11562 (2016).
11. A. V. Kachynski, A. N. Kuzmin, P. N. Prasad, and I. I. Smalyukh, "Coherent anti-Stokes Raman scattering polarized microscopy of three-dimensional director structures in liquid crystals," *Appl. Phys. Lett.* **91**(15), 151905 (2007).
12. B. G. Saar, H.-S. Park, X. S. Xie, and O. D. Lavrentovich, "Three-dimensional imaging of chemical bond orientation in liquid crystals by coherent anti-Stokes Raman scattering microscopy," *Opt. Express* **15**(21), 13585–13596 (2007).
13. A. V. Kachynski, A. N. Kuzmin, P. N. Prasad, and I. I. Smalyukh, "Realignment-enhanced coherent anti-Stokes Raman scattering and three-dimensional imaging in anisotropic fluids," *Opt. Express* **16**(14), 10617–10632 (2008).
14. M. Zimmerley, R. Younger, T. Valenton, D. C. Oertel, J. L. Ward, and E. O. Potma, "Molecular Orientation in Dry and Hydrated Cellulose Fibers: A Coherent Anti-Stokes Raman Scattering Microscopy Study," *J. Phys. Chem. B* **114**(31), 10200–10208 (2010).
15. F. Munhoz, H. Rigneault, and S. Brasselet, "High Order Symmetry Structural Properties of Vibrational Resonances Using Multiple-Field Polarization Coherent Anti-Stokes Raman Spectroscopy Microscopy," *Phys. Rev. Lett.* **105**(12), 123903 (2010).
16. B. Chon, J. Truong, M. Hansen, J.-I. Hahm, and Y. J. Lee, "Position- and Polarization-Specific Waveguiding of Multi-Emissions in Single ZnO Nanorods," *ACS Photonics* **6**(6), 1416–1424 (2019).
17. G. de Vito, A. Bifone, and V. Piazza, "Rotating-polarization CARS microscopy: combining chemical and molecular orientation sensitivity," *Opt. Express* **20**(28), 29369–29377 (2012).
18. F.-Z. Z. Bioud, P. Gasecka, P. Ferrand, H. H. Rigneault, J. Duboisset, and S. Brasselet, "Structure of molecular packing probed by polarization-resolved nonlinear four-wave mixing and coherent anti-Stokes Raman-scattering microscopy," *Phys. Rev. A* **89**(1), 013836 (2014).
19. J. Duboisset, P. Berto, P. Gasecka, F.-Z. Bioud, P. Ferrand, H. Rigneault, and S. Brasselet, "Molecular Orientational Order Probed by Coherent Anti-Stokes Raman Scattering (CARS) and Stimulated Raman Scattering (SRS) Microscopy: A Spectral Comparative Study," *J. Phys. Chem. B* **119**(7), 3242–3249 (2015).
20. Y. J. Lee, "Determination of 3D molecular orientation by concurrent polarization analysis of multiple Raman modes in broadband CARS spectroscopy," *Opt. Express* **23**(22), 29279–29295 (2015).
21. H. Shimada, S. Nobukawa, T. Hattori, and M. Yamaguchi, "Wavelength dispersion of birefringence of oriented polyethylene films," *Appl. Opt.* **56**(13), 3806–3811 (2017).
22. M. Hoff and Z. Pelzbauer, "Birefringence and orientation of polyethylene zone-drawn under various thermomechanical conditions," *Polymer* **33**(19), 4158–4163 (1992).

23. D. Ait-Belkacem, A. Gasecka, F. Munhoz, S. Brustlein, and S. Brasselet, "Influence of birefringence on polarization resolved nonlinear microscopy and collagen SHG structural imaging," *Opt. Express* **18**(14), 14859–14870 (2010).
24. F. Munhoz, H. Rigneault, and S. Brasselet, "Polarization-resolved four-wave mixing microscopy for structural imaging in thick tissues," *J. Opt. Soc. Am. B* **29**(6), 1541–1550 (2012).
25. R. P. Davis, A. J. Moad, G. S. Goeken, R. D. Wampler, and G. J. Simpson, "Selection rules and symmetry relations for four-wave mixing measurements of uniaxial assemblies," *J. Phys. Chem. B* **112**(18), 5834–5848 (2008).
26. Y. Liu, Y. Lee, and M. Cicerone, "Fast extraction of resonant vibrational response from CARS spectra with arbitrary nonresonant background," *J. Raman Spectrosc.* **40**(7), 726–731 (2009).
27. Y. Liu, Y. J. Lee, and M. T. Cicerone, "Broadband CARS spectral phase retrieval using a time-domain Kramers-Kronig transform," *Opt. Lett.* **34**(9), 1363–1365 (2009).
28. C. H. Camp, Y. J. Lee, and M. T. Cicerone, "Quantitative, comparable coherent anti-Stokes Raman scattering (CARS) spectroscopy: correcting errors in phase retrieval," *J. Raman Spectrosc.* **47**(4), 408–415 (2016).
29. D. A. Long, *Raman Spectroscopy* (McGraw-Hill, New York, 1977).
30. M. A. Yuratich and D. C. Hanna, "Coherent anti-Stokes Raman spectroscopy (CARS)," *Mol. Phys.* **33**(3), 671–682 (1977).
31. R. Brakel and F. W. Schneider, "Polarization CARS Spectroscopy," in *Advances in Non-linear Spectroscopy*, R. J. H. Clark and R. E. Hester, eds. (John Wiley & Sons, Chichester, UK, 1988), pp. 149–192.
32. Y. Saito, T. Ishibashi, and H. Hamaguchi, "Polarization-resolved coherent anti-Stokes Raman scattering (CARS) spectroscopy: a new probe of molecular symmetry through accurate determination of the Raman depolarization ratio," *J. Raman Spectrosc.* **31**(8-9), 725–730 (2000).